A new approach to the determinination of cardiac potential distributions: Application to the analysis of electrode configurations

Author

Johnston, Barbara M, Johnston, Peter R, Kilpatrick, David

Published

2006

Journal Title

Mathematical Biosciences

DOI

10.1016/j.mbs.2006.04.004

A New Approach to the Determination of Cardiac Potential Distributions: Application to the Analysis of Electrode Configurations*

Barbara M. Johnston and Peter R. Johnston†

School of Science,

Griffith University,

Nathan,

Queensland,

Australia, 4111,

Phone: 61–7–3735–7748,

Fax: 61–7–3735–7656,

E–mail: P.Johnston@griffith.edu.au

David Kilpatrick

Department of Medicine

University of Tasmania

GPO Box 252-34

Hobart

Tasmania

Australia 7001

January 23, 2006

*This work was supported by the Australian Research Council.

†Author to whom correspondence should be addressed.

Abstract

This paper presents a mathematical model and new solution technique for studying the electric potential in a slab of cardiac tissue. The model is based on the bidomain representation of cardiac tissue and also allows for the effects of fibre rotation between the epicardium and the endocardium. A detailed solution method, based on Fourier series and a simple one-dimensional finite difference scheme, for the governing equations for electric potential in the tissue and the blood, is also presented. This method has the advantage that the potential can be calculated only at points where it is required, such as the measuring electrodes. The model is then used to study various electrode configurations which have been proposed to determine cardiac tissue conductivity parameters.

Three electrode configurations are analysed in terms of electrode spacing, placement position and the effect of including fibre rotation: the usual surface four-electrode configuration; a single vertical analogue of this and a two probe configuration, which has the current electrodes on one probe and the measuring electrodes on the other, a fixed distance away. It is found that including fibre rotation has no effect on the potentials measured in the first two cases; however, in the two probe case, non-zero fibre rotation causes a significant drop in the voltage measured. This leads to the conclusion that it is necessary to include the effects of fibre rotation in any model which involves the use of multiple plunge electrodes.

Keywords: Bidomain Model, Anisotropy, Fibre Rotation, Simulation, Conductivity Values, Point Electrodes.

1 Introduction

Considerable importance has long been attached to the accurate determination of cardiac electrical conductivities. In particular, cardiac tissue anisotropy plays a vital role in accurate electrographic studies, such as examining defibrillation efficacy [1, 2], propagation of excitation waves [3, 4] and modelling ST segment shift in subendocardial ischaemia [5, 6, 7].

However, few experimentally determined conductivities [8, 9, 10] have been published because of the difficulties, due to very small electrodes and electrode spacings, associated with the actual measurements. Clerc [11] was able to circumvent these difficulties by using indirect methods to find the conductivities from the measurements of intracellular and extracellular action potentials and by independently measuring the longitudinal and transverse action potential propagation velocities. Significant variations can be seen in the tissue conductivity values which have been reported.

In addition, a tissue model must be adopted to analyse the experimental measurements and produce estimates of the cardiac conductivities. The generally accepted model is that of an anisotropic bidomain [12, 13, 14], consisting of intracellular and extracellular (interstitial) anisotropic domains, which can each be regarded as a continuum and which occupy the same space. The anisotropy comes partly from the differing electrical conductivity, both in the longitudinal and transverse directions, in each of the domains, and partly from the fact that the sheets of fibres rotate relative to one another as they move from the epicardium to the endocardium.

The bidomain model presented here is for a slab of cardiac tissue, stimulated by an external current source, and it is able to include the effects of fibre rotation. It is an extension of previous models for the left ventricle [5, 7], which looked at epicardial potential distributions arising from spatially varying transmembrane potentials. The solution method uses a Fourier

Series approach followed by a simple one-dimensional finite difference scheme. This allows both the intracellular and extracellular potentials to be evaluated only at points where they are required, rather than over the entire grid, as would be the case in a full numerical approach.

The model is then used to examine various electrode configurations that have been proposed to determine the cardiac tissue conductivities at a local (*in vivo*) level. These configurations are all based on the four-electrode technique, which uses a system of four equally spaced collinear electrodes on a single probe to measure the potential, on the inner two electrodes, produced by a current injected through the outer two electrodes. This technique has been used extensively to either measure or propose measurement systems for the cardiac conductivities [15, 16, 17, 18, 10, 19, 20].

Van Oosterom *et al.* [16] inserted a four-electrode probe perpendicularly into the myocardial wall but interpreted the results using an anisotropic monodomain model. Plonsey and Barr [17] placed a four-electrode probe on the epicardium, both along and at right angles to the cardiac fibres and, by assuming equal directional anisotropy ratios, were able to obtain analytical solutions for the potential along the probe. From these solutions they proposed using two types of electrode spacings: 'closely-spaced' where the electrode spacing is less than the space constant of the fibres and 'widely-spaced' where it is much greater than the space constant. This is due to the fact that the current is re-directed from the extracellular space to the intracellular space as the electrode spacing is increased, allowing the extracellular conductivities to be isolated from the intracellular conductivities in the 'closely-spaced' case.

An extension of Plonsey and Barr's [17] idea by Le Guyader *et al.* [19] involves again using a surface probe, which consists of two orthogonal rows of four electrodes [21], where the electrode spacing is of the order of the space constant. In this case, the current flow is re-directed between domains by increasing the frequency of the injected AC current. The conductivity parameters are calculated using a minimisation procedure.

Recently, Barr and Plonsey [20] have proposed the use of a single perpendicularly inserted probe, containing nine electrodes, some of which are extracellular electrodes and others of which are optical transmembrane potential sensors. This system would be used to determine membrane resistance as well as cardiac conductivities. The probe contains both 'closely-spaced' and 'widely-spaced' electrode sets. Analytical solutions for the potentials measured are found under the equal anisotropy ratios assumption.

This paper studies the effect that including fibre rotation will have on the potentials measured, for three different electrode configurations: the surface four-electrode probe [17]; a single vertical four-electrode probe [16] and a new two probe configuration, based on the single vertical probe, which has the current electrodes on one probe and the measuring electrodes on the other. These potential measurements are obtained for various values of fibre rotation and also probe insertion depth (for the latter two cases).

2 Description of the Model

This paper considers a block of cardiac tissue, finite in the x and y directions, with a length of $2L$ in each direction and extending from a plane at $z = 0$, which represents the epicardium, to a plane at $z = 1$, which represents the endocardium. The endocardium is assumed to be in contact with a volume of blood which extends to infinity in the positive z direction.

2.1 Governing Equations

The bidomain model [12] is used to account for the effects in both the intracellular and extracellular regions of the cardiac tissue. Here a direct current approach to the bidomain model is considered, but cardiac fibre rotation is also allowed for.

The governing equations for the intracellular potential, ϕ_i, and the extracellular potential,

ϕ_e, at the point $\mathbf{r} = (x, y, z)$ for an external current source per unit volume, $I_s = I_0\delta(\mathbf{r} - \mathbf{r_0})$ of amplitude I_0 injected at the point $\mathbf{r_0} = (x_0, y_0, z_0)$, are given by the following pair of coupled partial differential equations [19]:

$$\nabla \cdot [\mathbf{M}_i \nabla \phi_i(\mathbf{r})] = \frac{\beta}{R} [\phi_i(\mathbf{r}) - \phi_e(\mathbf{r})] \tag{1}$$

$$\nabla \cdot [\mathbf{M}_e \nabla \phi_e(\mathbf{r})] = -\frac{\beta}{R} [\phi_i(\mathbf{r}) - \phi_e(\mathbf{r})] - I_0\delta(\mathbf{r} - \mathbf{r_0}) \tag{2}$$

where β is the surface to volume ratio of the cells and R is the specific resistance of the membrane separating the intra- and extracellular domains. The intra- and extracellular conductivity tensors, $\mathbf{M}_i$ and $\mathbf{M}_e$, defined below, reflect the anisotropy of the cardiac tissue.

In addition, the electric potential in the blood, ϕ_b, is governed by Laplace's equation, since the blood is a source-free region, and so

$$\nabla^2 \phi_b = 0 \tag{3}$$

2.2 Conductivity Tensor

Cardiac tissue anisotropy comes both from the effect of the fibrous nature of the tissue, which allows current to flow more easily along the fibres (longitudinally) than across them (transversely), as well as the fact that the sheets of fibres rotate relative to one another as they move from the epicardium to the endocardium.

Here four conductivity values, g_{il}, g_{it}, g_{el} and g_{et}, are required to allow for differing conductivities in the two regions (l=longitudinal, t=transverse, i=intracellular, e=extracellular), since it is assumed that the two transverse dimensions (y and z) have the same conductivities. In addition, to describe the fibre rotation, it will be assumed that the fibres rotate anticlockwise from the epicardium to the endocardium, that the rotation varies linearly with depth [22] and that the fibre layers are parallel to the epicardium [23]. In addition, the model assumes that the fibres on the epicardium are aligned with the positive x-axis.

The preferred current path and fibre rotation are allowed for in the conductivity tensors $\mathbf{M}_i$ and $\mathbf{M}_e$ which appear in governing equations (1) and (2). Based on the above discussion the tensors will be of the following form [5]:

$$\mathbf{M}_q(z) = \begin{pmatrix} (g_{ql} - g_{qt})c^2 + g_{qt} & (g_{ql} - g_{qt})cs & 0 \\ (g_{ql} - g_{qt})cs & (g_{ql} - g_{qt})s^2 + g_{qt} & 0 \\ 0 & 0 & g_{qt} \end{pmatrix} \tag{4}$$

where $q = i$ or e (for intracellular and extracellular), $c = \cos \alpha z$, $s = \sin \alpha z$ and α is the total fibre rotation angle through the tissue. For the left ventricle, rotations in fibre direction have been reported in the range $103 \pm 21^\circ$ [24] up to 180° [25]. It should be noted that when fibre rotation is ignored, that is when $\alpha \equiv 0$, the conductivity tensors become for q=i or e,

$$\mathbf{M}_q(z) = \begin{pmatrix} g_{ql} & 0 & 0 \\ 0 & g_{qt} & 0 \\ 0 & 0 & g_{qt} \end{pmatrix} \tag{5}$$

and governing equations (1) and (2) reduce to the simplified bidomain equations [19]:

$$g_{il}\frac{\partial^2 \phi_i}{\partial x^2} + g_{it}\frac{\partial^2 \phi_i}{\partial y^2} + g_{it}\frac{\partial^2 \phi_i}{\partial z^2} = \frac{\beta}{R}(\phi_i - \phi_e) \tag{6}$$

$$g_{el}\frac{\partial^2 \phi_e}{\partial x^2} + g_{et}\frac{\partial^2 \phi_e}{\partial y^2} + g_{et}\frac{\partial^2 \phi_e}{\partial z^2} = -\frac{\beta}{R}(\phi_i - \phi_e) - I_s \tag{7}$$

2.3 Boundary Conditions

The following set of boundary conditions is used with governing equations (1), (2) and (3) to solve the model. Firstly, it is assumed that the epicardium is insulated, which gives

$$\frac{\partial \phi_i}{\partial z} = \frac{\partial \phi_e}{\partial z} = 0 \text{ at } z = 0 \tag{8}$$

Secondly, there is continuity of extracellular potential and current at the interface between the tissue and the blood; that is,

$$\phi_e = \phi_b \text{ at } z = 1, \text{ and} \tag{9}$$

$$g_b \frac{\partial \phi_b}{\partial z} = g_{et} \frac{\partial \phi_e}{\partial z} \text{ at } z = 1 \tag{10}$$

where g_b is the electrical conductivity in the blood, taken to be 6.7mS/cm here. Thirdly, the intracellular space is insulated by the extracellular space [26], which gives

$$\frac{\partial \phi_i}{\partial z} = 0 \text{ at } z = 1 \tag{11}$$

Also, since the blood mass is assumed infinite in the positive z-direction, $\phi_b \to 0$ as $z \to \infty$. Finally, the x and y boundaries of the domain are insulated, so the derivatives of ϕ_i, ϕ_e and ϕ_b in the x and y directions at these boundaries are zero.

3 Solution Method

Plonsey and Barr [17] solved the simplified bidomain equations (6) and (7) analytically for potential, for a four-electrode probe set on the surface of the cardiac region, under the assumption of equal directional anisotropy ratios [27]; that is, $\frac{g_{il}}{g_{el}} = \frac{g_{it}}{g_{et}}$. Le Guyader *et al.* [19] removed this restriction for the same electrode configuration but used an alternating current approach and a numerical method, based on the Fast Fourier Transform technique, to find the potential distribution for a given frequency, using equations (6) and (7). Recently, Barr and Plonsey [17] also found analytic solutions for potential for a vertical probe, again assuming equal directional anisotropy ratios.

Here, a Fourier Series approach, followed by a simple one-dimensional finite difference method, is employed to solve the more general bidomain equations (1), (2) and (3), which include cardiac fibre rotation, subject to boundary conditions (8)-(11). This approach has the advantage that the potential is calculated only at points where it is required.

Equations (1) and (2) can be written explicitly as:

$$M_i^{11} \frac{\partial^2 \phi_i}{\partial x^2} + 2M_i^{12} \frac{\partial^2 \phi_i}{\partial x \partial y} + M_i^{22} \frac{\partial^2 \phi_i}{\partial y^2} + M_i^{33} \frac{\partial^2 \phi_i}{\partial z^2} = \frac{\beta}{R} (\phi_i - \phi_e) \tag{12}$$

$$M_e^{11}\frac{\partial^2\phi_e}{\partial x^2}+2M_e^{12}\frac{\partial^2\phi_e}{\partial x\partial y}+M_e^{22}\frac{\partial^2\phi_e}{\partial y^2}+M_e^{33}\frac{\partial^2\phi_e}{\partial z^2}=-\frac{\beta}{R}\left(\phi_i-\phi_e\right)-I_0\delta(\mathbf{r}-\mathbf{r_0}) \qquad (13)$$

where M_q^{ab} $(a,b=1,2,3)$ represents the elements of the conductivity tensor matrices $\mathbf{M}_q(q=i,e)$. Recall that M_q^{11}, M_q^{12} and M_q^{22} are functions of z, via the fibre rotation, but M_q^{33} are constant.

3.1 Exploiting the Periodicity of the Geometry

The first step is to exploit the periodic nature of the potential functions, in both the x and y directions, by expanding each of the functions ϕ_i and ϕ_e in terms of a Fourier series:

$$\begin{aligned}\phi_q(\mathbf{r}) &= \sum_{n=0}^{\infty}\sum_{m=0}^{\infty}[C_{nm}^q(z)\cos m\pi y\cos n\pi x+D_{nm}^q(z)\sin m\pi y\cos n\pi x\\ &\quad +E_{nm}^q(z)\cos m\pi y\sin n\pi x+F_{nm}^q(z)\sin m\pi y\sin n\pi x]\\ &= C_{00}^q(z)+\sum_{m=1}^{\infty}[C_{0m}^q(z)\cos m\pi y+D_{0m}^q(z)\sin m\pi y]\\ &\quad +\sum_{n=1}^{\infty}[C_{n0}^q(z)\cos n\pi x+E_{n0}^q(z)\sin n\pi x]\\ &\quad +\sum_{n=1}^{\infty}\sum_{m=1}^{\infty}[C_{nm}^q(z)\cos m\pi y\cos n\pi x+D_{nm}^q(z)\sin m\pi y\cos n\pi x+\\ &\quad +E_{nm}^q(z)\cos m\pi y\sin n\pi x+F_{nm}^q(z)\sin m\pi y\sin n\pi x]\end{aligned} \qquad (14)$$

The aim now is to find the coefficient functions C_{00}^q, C_{0m}^q, D_{0m}^q, C_{n0}^q, E_{n0}^q, C_{nm}^q, D_{nm}^q, E_{nm}^q and F_{nm}^q, for $n,m=1,2,\ldots$. First substitute ϕ_i and ϕ_e from equation (14) into equation (12) and then equate the coefficients of the $\cos m\pi y\cos n\pi x$, $\sin m\pi y\cos n\pi x$, $\cos m\pi y\sin n\pi x$ and $\sin m\pi y\sin n\pi x$ terms. This gives four second order ordinary differential equations for each n,m combination. A similar substitution into equation (13) leads to four more differential equations. For each n and m, these eight differential equations can be divided into two sets of four equations each in four unknowns, where the first set involves the C_{nm}^q and F_{nm}^q coefficients and the second set involves the D_{nm}^q and E_{nm}^q coefficients ($q=i$ or e).

The C-F system is given by:

$$M_q^{33}\frac{d^2C_{nm}^q}{dz^2} - \left[n^2\pi^2M_q^{11} + m^2\pi^2M_q^{22} + \frac{\beta}{R}\right]C_{nm}^q + \frac{\beta}{R}C_{nm}^{q^*} + 2nm\pi^2M_q^{12}F_{nm}^q + \delta_{eq}I_0P_nR_m\delta(z-z_0) = 0 \tag{15}$$

$$M_q^{33}\frac{d^2F_{nm}^q}{dz^2} - \left[n^2\pi^2M_q^{11} + m^2\pi^2M_q^{22} + \frac{\beta}{R}\right]F_{nm}^q + \frac{\beta}{R}F_{nm}^{q^*} + 2nm\pi^2M_q^{12}C_{nm}^q + \delta_{eq}I_0Q_nS_m\delta(z-z_0) = 0 \tag{16}$$

where P_n, Q_n, R_m and S_m are defined below, q=i,e $\Leftrightarrow$ q^*=e,i and

$$\delta_{eq} = \begin{cases} 1 & q{=}e \\ \\ 0 & q{=}i, \end{cases} \tag{17}$$

The D-E system of 4 equations is of similar form to the above system and can be obtained by replacing C by D, F by E, P_nR_m by P_nS_m and Q_nS_m by Q_nR_m.

Although the C-F and D-E systems of differential equations apply for all $n, m \geq 0$, it is worth noting that there are fewer and simpler equations when either n or m is equal to 0. The equations are now decoupled and as can be seen from equation (14), for n=0 only the C and D coefficients are involved, for m=0 only the C and E coefficients are involved, while for $n = m$=0 there are only C coefficients. The appropriate equations for these coefficients can be found by setting n or m or both to zero in equations (15), (16) or their counterparts in D or E.

In the above analysis, the current term $I_0\delta(\mathbf{r}-\mathbf{r_0})$ in equation (13) is dealt with in a similar fashion to the potential terms by writing $I_0\delta(\mathbf{r}-\mathbf{r_0}) = I_0\delta(x-x_0)\delta(y-y_0)\delta(z-z_0)$ and then expanding each of $\delta(x-x_0)$ and $\delta(y-y_0)$ in a Fourier series:

$$\delta(x-x_0) = \sum_{n=0}^{\infty}(P_n\cos n\pi x + Q_n\sin n\pi x) = P_0 + \sum_{n=1}^{\infty}(P_n\cos n\pi x + Q_n\sin n\pi x) \tag{18}$$

and evaluating the coefficients using the fact that

$$\int_{-1}^{1}\delta(x-x_0)\cos n'\pi x\ dx = \begin{cases} 1 & n'{=}0, \\ \\ \cos n'\pi x_0 & n' \geq 1. \end{cases} \tag{19}$$

and

$$\int_{-1}^{1} \delta(x-x_0)\sin n'\pi x \; dx = \begin{cases} 0 & n'=0, \\ \\ \sin n'\pi x_0 & n' \geq 1. \end{cases} \tag{20}$$

This gives $P_0=\frac{1}{2}$, $P_n = \cos n\pi x_0$ and $Q_n = \sin n\pi x_0$. Similarly, writing

$$\delta(y-y_0) = R_0 + \sum_{m=1}^{\infty} (R_m \cos m\pi y + S_m \sin m\pi y) \tag{21}$$

gives $R_0=\frac{1}{2}$, $R_m = \cos m\pi y_0$ and $S_m = \sin m\pi y_0$.

The potential in the blood, ϕ_b, is also expanded in a Fourier series. However, in this case, since the medium is isotropic, symmetry allows it to be expanded in the shorter form

$$\phi_b = \sum_{n=1}^{\infty}\sum_{m=1}^{\infty} \Phi_b(m,n,z)\cos n\pi x \cos m\pi y \tag{22}$$

Substituting for ϕ_b into Laplace's equation (3) and noting that $\phi_b \to 0$ as $z \to \infty$, leads to a solution of the form

$$\phi_b = \sum_{n=1}^{\infty} \Omega_{n0} e^{-n\pi z}\cos n\pi x + \sum_{m=1}^{\infty} \Omega_{0m} e^{-m\pi z}\cos m\pi y + \sum_{n=1}^{\infty}\sum_{m=1}^{\infty} \Omega_{nm} e^{-\pi(n^2+m^2)^{\frac{1}{2}}z}\cos n\pi x \cos m\pi y \tag{23}$$

for constants Ω_{nm}. Note that when $n = m = 0$, $\phi_b = 0$.

3.2 Application of the Boundary Conditions

When the boundary conditions at the epicardium in equation (8) are applied to equation (14), it is found that for $q=i, e$:

$$\left.\frac{dC^q_{nm}(z)}{dz}\right|_{z=0} = \left.\frac{dD^q_{nm}(z)}{dz}\right|_{z=0} = \left.\frac{dE^q_{nm}(z)}{dz}\right|_{z=0} = \left.\frac{dF^q_{nm}(z)}{dz}\right|_{z=0} = 0 \tag{24}$$

In a similar fashion, boundary condition (11) at the endocardium leads to the following conditions, on the intracellular coefficients only:

$$\left.\frac{dC^i_{nm}(z)}{dz}\right|_{z=1} = \left.\frac{dD^i_{nm}(z)}{dz}\right|_{z=1} = \left.\frac{dE^i_{nm}(z)}{dz}\right|_{z=1} = \left.\frac{dF^i_{nm}(z)}{dz}\right|_{z=1} = 0 \tag{25}$$

Applying boundary conditions (9) and (10) implies that the extracellular coefficients for D, E and F and their derivatives are equal to 0 at the endocardium. The derivative condition is ignored as it is redundant, which leaves

$$D^e_{nm}(1) = E^e_{nm}(1) = F^e_{nm}(1) = 0 \tag{26}$$

However, when equations (9) and (10) are applied to the C^e_{nm} coefficients, the result is different because the coefficients of the $\cos n\pi x \cos m\pi y$ terms in expansion (22) for ϕ_b match the C^e_{nm} coefficients in the ϕ_e expansion (14). The relevant boundary conditions are:

$$\left.\frac{dC^e_{nm}(z)}{dz}\right|_{z=1} = \frac{g_b}{g_{et}}\left[-\pi(n^2+m^2)^{\frac{1}{2}}\right] C^e_{nm}(1) \text{ and } C^e_{nm}(1) = \Omega_{nm} e^{-\pi(n^2+m^2)^{\frac{1}{2}}} \tag{27}$$

It should be noted that boundary conditions (24)-(27) apply for all $n, m \geq 1$ and are also correct, where appropriate, for n or m equal to 0; that is, for C^q_{0m} and D^q_{0m} for $n = 0$ and for C^q_{n0} and E^q_{n0} for $m = 0$ (see equation (14)). The equivalent conditions for $n = m = 0$, where ϕ_b=0, are :

$$C^e_{00}(1) = 0 \text{ and } \left.\frac{dC^e_{00}(z)}{dz}\right|_{z=1} = 0 \tag{28}$$

3.3 Finite Difference Scheme

Next, a one-dimensional finite difference scheme is applied to the eight ordinary differential equations which result from the initial governing equations. A non-uniform grid is used so that it is possible to cluster points near the current source. The interval between 0 and 1 in the z-direction is divided into n sub-intervals of differing lengths $\Delta z_k = z_k - z_{k-1}$ at z_0=0, z_1, $\cdots$, z_N=1. For a function $f(z)$ defined on this grid, $f_k = f(z_k)$, applying Taylor series expansions gives the following approximations for $k = 0, \ldots, N$:

$$\left.\frac{d^2 f}{dz^2}\right|_{z=z_k} \approx \frac{2(\Delta z_{k+1} f_{k-1} - (\Delta z_k + \Delta z_{k+1}) f_k + \Delta z_k f_{k+1})}{\Delta z_k \Delta z_{k+1}(\Delta z_k + \Delta z_{k+1})} \tag{29}$$

and

$$\left.\frac{df}{dz}\right|_{z=z_k} \approx \frac{f_{k+1} - f_{k-1}}{\Delta z_k + \Delta z_{k+1}} \tag{30}$$

For the case where $n, m \geq 1$, these approximations are applied to the two sets of four equations, the C-F system given by equations (15) and (16) and the D-E system described below those equations, as well as to boundary conditions (24)-(27). This gives, for each n and m, sets of four banded diagonal systems of linear algebraic equations of size $4N+3$ for the C-F system and $4N+2$ for the D-E system, with a band-width of 9 in each case. The systems are different sizes because for $n, m \geq 1$, $X^e_{nm}(1)=0$ for $X=D$, E and F, but not for C, as can be seen in equations (26) and (27). This eliminates the equations for $k=N$ for D^e_{nm} and E^e_{nm} in the D-E system, but in the C-F system only the F^e_{nm} equation is eliminated.

As previously discussed in Section 3.1, when $n=0$, equations (15) and (16) decouple, leaving two sets of two equations in four unknowns for the C system (size $2N+2$) and the F system (size $2N+1$) and similarly for C and E when $m=0$. Finally, when $n=m=0$, the C system has size $2N+1$.

The current term of equations (15) and (16) when $q=e$, which involves the Dirac delta function $\delta(z - z_k)$, is evaluated in the right-hand side vector in the algebraic system as, for example in equation (15), $\frac{-I_0 P_n R_m}{\Delta z_k}$ when $k \neq 0$. However, when $k=0$, this is doubled because the current is being applied on the epicardium and the solution of the equations is based on the assumption that the medium is infinite in extent, whereas in that case it is semi-infinite [17].

In order to apply the above work in a realistic fashion and compare theoretical results with experimentally measured data, it is necessary to have both a current source and a sink. To allow for this, the model is solved with an extra current term of the same magnitude but opposite in sign, which is applied at a different point from $\mathbf{r}_0$. This simply introduces an extra term in governing equation (2) and hence in the algebraic system. The extra term was ignored in the

work above to simplify the analysis.

For each value of n and m the banded systems of algebraic equations are solved using standard techniques [28] to give values for the coefficients $C^q_{nm}(z)$, $D^q_{nm}(z)$, $E^q_{nm}(z)$ and $F^q_{nm}(z)$ at the required points z. Finally, summing the series in (14) for sufficiently many points NPTSx and NPTSy, for n and m respectively, yields the potential. Unless otherwise stated, the model was solved with NPTSx=NPTSy=N=200, where N is the number of points in the z-direction.

It was also found that it was necessary to include an accelerator term in the series summation to counteract the Gibbs effect [29]. Lanczos smoothing [29], which multiples each term in the series summed over n, by the factor $\frac{\sin(\frac{\pi n}{\mathrm{NPTS}x})}{\frac{\pi n}{\mathrm{NPTS}x}}$, was applied; here, since there are two series to be summed, each term in the series was multiplied by a product of this factor and a similar one in m before the summation was performed.

4 Validation of the Model

4.1 Isotropic Case

As discussed in Section 2.2, when fibre rotation is ignored, governing equations (1) and (2) reduce to the simpler form of equations (6) and (7). If, in addition, it is assumed that the medium is isotropic, that is, the conductivities are all equal, then it is possible to solve the equations analytically.

First set $g_{ql} = g_{qt} = g$ for q=i or e. Also to simplify the algebra, current is applied via a vertical probe inserted at the point $x_0 = y_0 = 0$. In this case, the two systems of four equations, in (15) and (16) and below them, reduce to the following pair of coupled ordinary differential equations for $y_i = C^i_{nm}$ and $y_e = C^e_{nm}$ with n and m not both 0:

$$\frac{d^2 y_i}{dz^2} - (a+b)y_i + by_e = 0 \tag{31}$$

$$\frac{d^2y_e}{dz^2} - (a+b)y_e + by_i + I_0\delta(z-z_0)/g = 0 \tag{32}$$

where $a = \pi^2(n^2+m^2)$ and $b = \frac{\beta}{gR}$ since $P_n = R_m = 1$ for $x_0 = y_0 = 0$. The boundary conditions (8)-(11) become $y_i^{'}(0) = y_e^{'}(0) = 0$, $y_i^{'}(1) = 0$ and $y_e^{'}(1) = -\sqrt{a}Gy_e(1)$ where $G = \frac{g_b}{g}$.

This system involves only the C_{nm}^i and C_{nm}^e coefficients because $D_{nm}^i = D_{nm}^e = E_{nm}^i = E_{nm}^e = F_{nm}^i = F_{nm}^e = 0$ here. This can be seen from the fact that the equations for these coefficients are the same as those above, except that the current terms are equal to 0 because $Q_n = S_m = 0$ for $x_0 = y_0 = 0$. This leads to $y_i = y_e = 0$ for the system when the boundary conditions $y_i^{'}(0) = y_e^{'}(0) = 0$ and $y_i{}^{'}(1) = y_e^{'}(1) = 0$ are applied.

The system given above is solved in two regions and the solutions are matched at the point of current application z_o to find the values of the unknown constants. This method gives, for $z \leq z_0$:

$$\begin{aligned} y_i &= A_1\cosh kz + C_1\cosh lz \\ y_e &= A_1\cosh kz - C_1\cosh lz \end{aligned} \tag{33}$$

where $k^2 = a$ and $l^2 = a+2b$; whereas for $z \geq z_0$:

$$\begin{aligned} y_i &= A_2\cosh kz + B_2\sinh kz + C_2\cosh lz + D_2\sinh lz \\ y_e &= A_2\cosh kz + B_2\sinh kz - C_2\cosh lz - D_2\sinh lz \end{aligned} \tag{34}$$

where it can be shown that

$B_2 = \frac{I_0\cosh kz_0}{2kg}$, $D_2 = -\frac{I_0\cosh lz_0}{2lg}$, $C_2 = \frac{\cosh lz_0[2l\cosh l\sinh k + G(l\cosh l\cosh k + k\sinh k\sinh l)] - Gl\cosh kz_0}{4l^2\sinh k\sinh l + 2Gl(l\sinh l\cosh k + k\sinh k\cosh l)}$,

$A_2 = -\frac{[kB_2\cosh k + lC_2\sinh l + lD_2\cosh l]}{k\sinh k}$, $C_1 = C_2 + D_2\tanh lz_0$ and $A_1 = A_2 + B_2\tanh kz_0$.

The numerical model was found to give excellent agreement with the analytic solution for particular values of n and m, not both 0. The case where $n = m = 0$ is different from the above because, although most of the boundary conditions are the same, in that case $y_e(1) = 0$. It is, however, a special case of the scenario discussed in the next section and so it will be covered below.

4.2 C^i_{00} and C^e_{00} coefficients

This section checks the numerical model for the C_{00} coefficients only, for the case where the medium need not be isotropic. Again an analytic solution can be found for the coefficients for comparison with numerical results.

When n=m=0, the only coefficients involved are the C^i_{00} and C^e_{00} coefficients, as explained in Section 3.1, and denoting these here as y_i and y_e respectively, gives the following pair of coupled ordinary differential equations for $y_i = C^i_{00}$ and $y_e = C^e_{00}$:

$$\frac{d^2 y_i}{dz^2} - a_i y_i + a_i y_e = 0 \tag{35}$$

$$\frac{d^2 y_e}{dz^2} - a_e y_e + a_e y_i + I_0 \delta(z - z_0)/(4g_{et}) = 0 \tag{36}$$

since P_0=R_0=$\frac{1}{2}$. Here $a_i = \frac{\beta}{Rg_{it}}$ and $a_e = \frac{\beta}{Rg_{et}}$.

The boundary conditions (24), (25) and (28) become $y_i^{'}(0) = y_e^{'}(0) = 0$, $y_i^{'}(1) = 0$ and $y_e(1) = 0$. This system is solved in a similar fashion to the equations in the previous section and compared with the numerical solution for both the isotropic and non-isotropic cases. Notice that it it not necessary to assume that a particular vertical electrode is used, as in the previous section, since only the C^i_{00} and C^e_{00} coefficients are involved and P_0=R_0=$\frac{1}{2}$ for all values of x_0 and y_0. Again excellent agreement is found between the analytic solution and the numerical model.

4.3 The Four-Electrode Model of Plonsey and Barr (Surface Probe)

In this section, results from the numerical model are compared with the analytical solutions of Plonsey and Barr [17], who use a four-electrode method, which consists of a probe containing four equi-spaced electrodes, the outer two of which carry an applied current, while the inner two measure the resulting voltage. Their method involves a direct current applied to a surface

(horizontal) probe (Figure 1) under the assumption of equal directional anisotropy ratios; that is,

$$\frac{g_{il}}{g_{el}} = \frac{g_{it}}{g_{et}} = k \tag{37}$$

where k is a constant. The simplified governing equations are given by (6) and (7), where the parameters are β=2000 cm^{-1} and R=2000 Ω cm^2 and the conductivity values are taken to be g_{il}=0.00343 S/cm, g_{el}=0.00625 S/cm, g_{it}=0.000596 S/cm and g_{et}=0.00109 S/cm [17], based on the measurements of Clerc [11], but constrained by the need to satisfy the equal directional anisotropy ratios condition. This gives k=0.549. The probe is applied along the x-direction (longitudinal), where y_0=z_0=0, or the y-direction (transverse), where x_0=z_0=0, and it is assumed that conductivity is the same in the y and z directions.

Plonsey and Barr [17] find analytic solutions for potential from the governing equations by applying the scale transformations $X = \frac{x}{\sqrt{g_{il}}}$, $Y = \frac{y}{\sqrt{g_{it}}}$ and $Z = \frac{z}{\sqrt{g_{it}}}$. They define space constants in the longitudinal and transverse directions as $\lambda_l = \sqrt{g_{il}}\lambda$ and $\lambda_t = \sqrt{g_{it}}\lambda$ respectively, in terms of the space constant $\lambda = \sqrt{\frac{R}{(1+k)\beta}}$. This gives λ_l=0.470 mm and λ_t=0.196 mm.

If the variable W is used to denote the direction (l or t) along which the electrodes are placed, the current source is at $W = -P$ and the sink is at $W = P$, then the potential is given by [30]:

$$\phi_i(w) = \frac{-I_0}{2\pi g\lambda}\left(\frac{k}{k+1}\right)\left[\left(\frac{e^{-|w+p|}}{|w+p|} - \frac{e^{-|w-p|}}{|w-p|}\right) + \frac{1}{|w-p|} - \frac{1}{|w+p|}\right] \tag{38}$$

and

$$\phi_e(w) = \frac{I_0}{2\pi g\lambda}\left(\frac{k}{k+1}\right)\left[k\left(\frac{e^{-|w+p|}}{|w+p|} - \frac{e^{-|w-p|}}{|w-p|}\right) + \frac{1}{|w+p|} - \frac{1}{|w-p|}\right] \tag{39}$$

where $w = W/\lambda_w$, $p = P/\lambda_w$ and $g = g_{it}\sqrt{g_{il}}$.

Three distinct situations can be identified depending on the magnitude of the position P of the electrodes relative to λ_w: $P = 0.1\lambda_w$; $P = \lambda_w$ and $P = 5\lambda_w$, where, as the inter-electrode spacing increases, the current moves from flowing only in the extracellular space to flowing in

both spaces.

For the numerical model, consideration of the form of the Fourier expansions for potential (14), shows that for a surface probe, where y=z=0,

$$\begin{aligned}\phi_q(x) = C^q_{00}(0) + \sum_{m=1}^{\infty} C^q_{0m}(0) + \sum_{n=1}^{\infty} [C^q_{n0}(0)\cos n\pi x + E^q_{n0}(0)\sin n\pi x] \\ + \sum_{n=1}^{\infty}\sum_{m=1}^{\infty} [C^q_{nm}(0)\cos n\pi x + E^q_{nm}(0)\sin n\pi x]\end{aligned} \tag{40}$$

so that only the $C^q_{nm}(0)$ and $E^q_{nm}(0)$ coefficients must be found.

The numerical model was used to produce graphs of potential to compare with Plonsey and Barr's analytic solutions for the three cases of electrode spacing mentioned above [17, 30]. A comparison plot is shown in Figure 2 for the case where the electrode spacing is much larger than the space constant; that is $P = 5\lambda_w$, so that the current electrodes are placed at positions of ± 5 in λ_w units and the measuring electrodes are at $\pm\frac{5}{3}$ units. The graphs are for normalised intra- and extracellular potential (scaled by the factor $\frac{I_0}{2\pi\lambda g}$) plotted against position in λ_w units. Note that the graphs are identical for w=l or t due to the scaling.

For the three cases of electrode spacing, the graphs show excellent agreement between the analytic solution and the numerical model at the measuring electrodes and across the majority of the length of the probe, except in the vicinity of the source and sink, where the peak value for the numerical model is less than the peak analytical value. In all three cases, the relative errors between the analytic and numerical values are less than 1% at the measuring electrodes.

For the $P = 0.1\lambda_w$ case, P=0.047 mm in the longitudinal direction, giving a distance of about 30 μm between the measuring electrodes, which is at the microscopic level (10-100 μm) for cardiac cells [18]. To cope with this resolution, it is necessary to increase the number of terms in the Fourier Series summation and the vertical discretisation in the numerical model, that is, NPTSx = NPTSy = N, from 200, which was used for the other two cases, to 1000.

Le Guyader *et al.* [19] also checked their model against Plonsey and Barr's [17] results. The

comparisons of potential were made only at the measuring electrodes and the parameters used were $\frac{g_{il}}{2}$, $\frac{g_{el}}{2}$, g_{it}, g_{et}, β, k and R from Plonsey and Barr (see above). The probe used by Le Guyader *et al.* [19, 21] had a length of $3d$, where d is the electrode spacing, with source/sink at $\pm\frac{3}{2}d$ and measuring electrodes at $\pm\frac{d}{2}$, compared with Plonsey and Barr's probe, where the source/sink separation was $2d$ and the measuring electrodes were at $\pm\frac{d}{3}$. Here the value of d is $\frac{\lambda_l}{\sqrt{2}}$=333 μm for the longitudinal orientation and 196 μm for the transverse orientation, using the above parameters. This means that the physical situation chosen by Le Guyader *et al.* corresponds to the scenario where current is flowing in both the intra- and extracellular spaces (see Section 4.2).

When the probe arrangement and parameter values of Le Guyader *et al.* are used in our model, as a comparison with the results of Plonsey and Barr [17], it is found that there is a maximum relative error in the potential difference of 1% in the longitudinal direction and 2.7% in the transverse direction with NPTSx=NPTSy=N=200, compared with 2.5% and 1% respectively found by Le Guyader *et al.* [19].

4.4 Barr and Plonsey's Vertical Electrode System

A recent paper by Barr and Plonsey [20] suggests the use of a combination of optical transmembrane potential sensors and extracellular electrodes on a single vertical probe to determine cardiac conductivities. Again the assumption of equal directional anisotropy ratios, as defined in equation (37), is made, to allow analytic solutions to be found for the potential at the measuring electrodes. The vertical probe (see Figure 3) contains nine electrodes numbered consecutively from top to bottom, with electrodes 1,2,6,7,8 and 9 each 200 μm apart, while electrodes 2,3,4,5 and 6 are only 50 μm apart.

By applying a two-phase protocol, Barr and Plonsey [20], show that, under the constant anisotropy assumption, it is theoretically possible to determine, firstly, the extra-cellular con-

ductivities (using the 'closely-spaced' electrode set 3-6, Figure 3(a)) and secondly, the intracellular conductivities (using the more 'widely-spaced' electrode set 1,2,6,8, Figure 3(b)). (Note that electrodes 7 and 9 are optical transmembrane potential sensors.) The relevant equations are found as linear combinations of the equations presented in Plonsey and Barr's 1982 paper [17]. The voltage between the two 'closely-spaced' electrodes 4 and 5, V_x^1, is given by

$$V_x^1 = \frac{I_0^a}{4\pi s\sqrt{g_{ox}g_{oz}}} \tag{41}$$

where I_0^a is the magnitude of the stimulus current between electrodes 3 and 6 and s is the electrode spacing. In their notation, conductivities, g, have subscripts indicating both the coordinate direction and the domain, with o for extracellular (interstitial) and i for intracellular.

The expression for the voltage between the 'widely-spaced' electrodes 2 and 8, where the current I_0^b is injected at electrodes 1 and 6, is

$$V_x^2 = \frac{I_0^b}{4\pi g}\left(\frac{k}{k+1}\right)\left[\frac{1+ke^{\frac{-R^{86}}{\lambda}}}{R^{86}} - \frac{1+ke^{\frac{-R^{81}}{\lambda}}}{R^{81}}\right] \tag{42}$$

where $g = \sqrt{g_{ix}g_{iy}g_{iz}}$ and the distance $|x_{pq}|$ along the x-axis between electrodes p and q is scaled as $R^{pq} = \frac{|x_{pq}|}{\sqrt{g_{ix}}}$.

The expressions for transmembrane potential, V_m^1 and V_m^2, measured at electrodes 7 and 9 respectively are

$$V_m^1 = \frac{-kI_0^b}{4\pi g}\left[\frac{e^{\frac{-R^{76}}{\lambda}}}{R^{76}} - \frac{e^{\frac{-R^{71}}{\lambda}}}{R^{71}}\right] \tag{43}$$

and

$$V_m^2 = \frac{-kI_0^b}{4\pi g}\left[\frac{e^{\frac{-R^{96}}{\lambda}}}{R^{96}} - \frac{e^{\frac{-R^{91}}{\lambda}}}{R^{91}}\right] \tag{44}$$

Values for V_x^1, V_x^2, V_m^1 and V_m^2 are calculated using the numerical model for comparison with the values from equations (41)-(44), using the tissue conductivities and constants of Barr and Plonsey [20]. Good agreement is found between the analytic and numeric values. For example, when the probe is placed with electrode number 1 at a vertical depth of 0.2 cm, the voltage

values agree to within 1.8% for V_x^1, 0.2% for V_x^2, 2.2% for V_m^1 and 0.4% for V_m^2, although for V_x^1, where the electrodes are only 50μm apart, it is necessary to increase the number of terms in the Fourier Series summation and the vertical discretisation from 200 to 1000 points to cope with the resolution.

It should be noted that the good agreement between the model values and the analytical values validates the numerical model calculations for both extracellular potential and intracellular potential since $V_m = \phi_e - \phi_i$.

5 Results

5.1 The Effect of Varying Conductivity Values

In this section, the potentials in the graphs from Section 4.3 are re-calculated using various values for the tissue conductivities, with the aim of determining the effect that these conductivity values have on the measured potential.

As pointed out by Roth [31], no consensus exists regarding the correct values of the bidomain conductivities, because of inconsistencies in the experimental data. This can be seen in columns 1 to 3 of Table 1, where the conductivity values of Clerc [11], Roberts *et al.* [8] and Roberts and Scher [9] are presented. Column 4 contains the means of columns 1 to 3.

Here, the mean value for g_{il} is used, in conjunction with Roth's [31] 'recipe', to derive consistent conductivity values which represent the three most commonly used modelling scenarios [31], viz., unequal anisotropy ratios ($g_{il}/g_{it} \neq g_{el}/g_{et}$), equal anisotropy ratios ($g_{il}/g_{it} = g_{el}/g_{et}$) and reciprocal anisotropy ratios ($g_{il}/g_{it} = g_{et}/g_{el}$), denoted here as 'nominal', 'equal' and 'reciprocal' respectively. In terms of Roth's [31] additional parameters the conductivity values for columns 5 to 7 are taken to be α=1 and $\frac{\lambda_l}{\lambda_t}$=2.5 with ϵ=0.75 (nominal), ϵ=1 (equal) and ϵ=0.9935 (reciprocal).

The four-electrode surface probe of Section 4.3, shown in Figure 1, is used in numerical simulations in conjunction with the three sets of conductivity values mentioned above to produce graphs of potential along the length of the probe. Here β=2000 cm^{-1} [17], R=9100 Ω cm^2 [32] and I_0=5 μA [20]. Graphs of scaled (by $\frac{I_0}{2\pi\lambda g}$) potential for the mean data set of column 4 are found to be almost identical to the nominal data set graphs and so these are not presented here. This is perhaps not surprising, given that the parameters for the mean data set are α=0.81, $\frac{\lambda_l}{\lambda_t}$=2.2 and ϵ=0.71 compared with 1, 2.5 and 0.75 respectively for the nominal data set.

The plot shown in Figure 4 for the $5\lambda_w$ case, where the electrodes are placed at positions of ± 5 in λ_w units, is very similar to that in Figure 2 from Section 4.3, except that, as expected, the magnitudes of the potentials differ slightly between the two figures, because the conductivity values used are different. In Figure 4 the three types of curves have the same general pattern but considerably different magnitudes, with the highest potentials produced by the equal data set and the lowest by the reciprocal data set.

Next, it would seem to be useful to consider actual, rather than scaled, potentials at the measuring electrodes to determine the effect of the various conductivity data sets on these readings. The actual voltages in millivolts are presented in Table 2. As expected, the extracellular potential (measured) drops as the electrode spacing is increased and the intracellular potential (not measured) increases. In addition, it is clear that the choice of conductivity values has a marked effect, that is up to two orders of magnitude, on the potentials which would be measured.

Finally, the same three scenarios are repeated, but this time the fibre rotation angle, defined in Section 2.2, is set to 120°. Not surprisingly, since the probe is on the epicardium, increasing the fibre rotation has no effect on the potentials at the measuring electrodes.

5.2 Vertical Probe Depth and Fibre Rotation

The scenario considered here is whether placing a single vertical probe deeper into the tissue will affect the numerical results and whether increasing fibre rotation has an effect on the potential measured. It is possible that potential measurements may be different when the probe is inserted deeper into the tissue because our model assumes that there is a volume of blood situated beneath the endocardium.

To do this, a vertical analogue [16] (see Figure 5) of the four-electrode configuration of Section 4.3 will be used. The distance between the current electrodes is taken to be 600 μm, the measuring electrodes are placed 200 μm apart and the nominal tissue conductivities and values for β, R and I_0 from Section 5.1 are used. Voltages are calculated for the top current electrode placed at depths of 3mm, 5mm and 7mm below the epicardium. It is found that there was no change in the potentials measured as the depth of the electrodes is increased.

Another consideration is the effect that fibre rotation may have on measured voltage when the probe is placed at different depths. The above simulations are repeated, this time with the fibre rotation angle, α, defined in Section 2.2, set to 0°, 60°, 120° and 180°. The maximum fibre rotation considered is 180°, as this is believed to be the highest degree of fibre rotation observed [25]. The measured potentials are not affected by the changes in α, which indicates that fibre rotation has no effect on voltage readings for the vertical probe. This result is consistent with the analysis of van Oosterom *et al.* [16] and can be explained by the fact the vertical probe forms an axis of rotation for the fibres.

5.3 Two Vertical Probes

Since it has been suggested [20] that it may be either desirable or even necessary to use multiple probes to fully determine the conductivity values, here the effect of increasing the distance

between the current electrodes, the 'probe spacing', and the measuring electrodes will be considered and the effect, if any, that fibre rotation may have on these voltage readings.

Here a new four-electrode configuration, shown in Figure 6, is used. It consists of two probes inserted into the cardiac tissue, normal to the epicardium, a fixed distance apart in the x-direction. The first probe contains the current source electrodes and the second the measuring electrodes.

Voltage values are calculated for probe spacings up to 0.1 cm, at depths of 0.2 cm and 0.7 cm for the top current electrode. These calculations are performed with and without 120° fibre rotation. The nominal conductivity values and tissue constants from Section 5.2 are again used here.

The graph in Figure 7 shows that the drop in voltages, between the zero and 120° fibre rotation cases, at 0.02 cm from the current electrodes is around 0.6 mV for the shallower probe and 2.4 mV for the deeper probe. The graphs show that, as expected, voltage decreases with increasing distance between the measuring electrodes and the current electrodes. However, it can also be seen that inclusion of fibre rotation has a significant effect on the magnitudes of the voltages measured, with lower voltages recorded when fibre rotation is allowed. In addition, the drop-off in voltage is more pronounced when the probe is placed deeper into the cardiac tissue.

This relationship between voltage measurements for various depths of the current electrodes and/or various degrees of the fibre rotation was the basis for the proposal of an in-principle method for determining cardiac fibre rotation. The method has been detailed elsewhere [33] and basically consists of using the model to produce a plot of potential difference versus fibre rotation for a given depth of the top current electrode. The plot is then used, in conjunction with potential measurements made at the same depth, to read off the fibre rotation.

6 Discussion

This paper has introduced a bidomain model to study various electrode configurations which have been proposed to determine cardiac tissue conductivities. The solution method employs a Fourier Series approach, followed by a simple one-dimensional finite difference method, to solve the bidomain equations which include cardiac fibre rotation and the potential is calculated only at points where it is required.

Three electrode scenarios are presented: the surface four-electrode probe of Plonsey and Barr [17]; a single vertical four-electrode of analogue of this [16] and a two vertical probe configuration, based on the single vertical probe case. The effect on the measured potentials of including fibre rotation is considered and it is found that, while fibre rotation has no effect on the voltage readings in the first two cases, it does have a measurable effect in the two vertical probe case, because the measuring electrodes are at a distance from the current electrodes. In addition, this effect is magnified when the probes are placed deeper into the cardiac tissue.

This finding is significant because if it is necessary for reasons such as model generality, redundancy or noise to obtain multiple measurements from an array of electrodes [20], then it is also necessary to take fibre rotation into account. This is contrary to previous suggestions [16] that for a vertical probe of length 1 mm, fibre rotation can be considered fairly uniform and therefore be ignored.

Another consideration here is the impact that different conductivity values have on the potentials which would be measured. For example, Plonsey and Barr assume equal directional anisotropy ratios for both their electrode scenarios [17, 20] in order to be able to find analytical expressions for the potentials, even though they admit that there are doubts about the validity of this [17, 14, 20]. Various experimental and modelling studies [34, 35, 36, 37, 38, 6, 7] have shown that it is necessary to use unequal anisotropy ratios to produce meaningful and realistic

potential distributions on the epicardium and in the thorax.

Here, simulations are carried out for the surface four-electrode model, firstly which mimic the three electrode spacing cases of Plonsey and Barr [17, 30], viz., spacing much less than, equal to or much greater than the space constant, not just for the equal anisotropy case but also for unequal anisotropy ratios and the reciprocal anisotropy case. These simulations confirm, for all three conductivity sets, the theoretical result that when the electrode spacing is much less than the space constant, that is the 'closely-spaced' electrode case, the current is flowing almost entirely in the extracellular domain and that there is a gradual flow into the intracellular domain as this spacing is increased. However, it can be seen that there is a significant difference in the magnitude of the potentials which would be measured, depending on the conductivity values which are used.

7 Conclusions

This paper has presented a new bidomain model of cardiac tissue, which is able to include the effects of the fibre rotation between the epicardium and the endocardium. The model has the advantage that potential can be calculated only at points where it is required, for example, at the measuring electrodes.

The model has been used to study various probe configurations, namely a four-electrode surface probe [17], a single four-electrode vertical probe [16] and two vertical probes, both with and without fibre rotation. It was found that including fibre rotation has no effect on the potential measured for the surface probe or the single vertical probe. However, if two vertical probes, where the current source and sink are at a distance from the measuring electrodes, are used, then increased fibre rotation causes a significant drop in the voltage readings and the degree of this effect is related to the depth of the probe.

The modelling studies with vertical electrodes presented here assume that: the electrodes can be inserted into the tissue without causing significant injury currents, which appears to be the case for the recently introduced silver wire plunge electrodes [39]; the size of the electrodes is insignificant compared with the inter-electrode distance; the fibre sheets are parallel to the epicardium, which means that the method cannot be applied near the base or apex of the heart, but only in the region [23] where this assumption is almost satisfied and that the fibre rotation varies linearly with depth, a common modelling assumption [22].

What has been shown here is that, if multiple vertical probes are to be used to experimentally determine the conductivity values, then it is essential that this be in conjunction with a model having an unconstrained anisotropy ratio that also allows for fibre rotation. In addition, simulations using three different but consistent sets of conductivities have shown that there are large differences in voltage readings for the various sets of conductivity data and this confirms the importance of an accurate determination of the conductivity values.

A further extension of the model to allow for stimulation at multiple frequencies may also be a useful development in the quest to determine the cardiac tissue conductivities.

References

[1] M. Malik, K. F. A. A. Smits, and F. W. Lindemans. Effects of anisotropic myocardial conductivity in model of defibrillation current density distribution. *Medical and Biological Engineering and Computing*, 32(4):34–40, 1994.

[2] C. Y. Wang and J. B. Bassingthwaighte. Capillary supply regions. *Mathematical Biosciences*, 173:103–114, 2001.

[3] R.C. Barr and R. Plonsey. Propagation of excitation in idealized anisotropic two–dimensional tissue. *Biophys. J.*, 45:1191–1202, 1984.

[4] M.S. Spach and R.C. Barr. Effects of cardiac microstructure on propagating electrical waveforms. *Circ. Res.*, 86:23–28, 2000.

[5] Peter R. Johnston, David Kilpatrick, and Chuan Yong Li. The importance of anisotropy in modelling ST segment shift in subendocardial ischaemia. *IEEE Transactions on Biomedical Engineering*, 48(12):1366–1376, December 2001.

[6] Peter R. Johnston and David Kilpatrick. The effect of conductivity values on ST segment shift in subendocardial ischaemia. *IEEE Transaction on Biomedical Engineering*, 50(2):150–158, February 2003.

[7] Peter R. Johnston. A cylindrical model for studying subendocardial ischaemia in the left ventricle. *Mathematical Biosciences*, 186(1):43–61, 2003.

[8] D. E. Roberts, L. T. Hersh, and A. M. Scher. Influence of cardiac fiber orientation on wavefront voltage, conduction velocity and tissue resistivity in the dog. *Circ. Res.*, 44:701–712, 1979.

[9] D. E. Roberts and A. M. Scher. Effects of tissue anisotropy on extracellular potential fields in canine myocardium in situ. *Circ. Res.*, 50:342–351, 1982.

[10] P. Le Guyader, P. Savard, and F. Trelles. Measurement of myocardial conductivities with an eight–electrode technique in the frequency domain. *17th IEEE-EMBS*, pages 71–72, 1995.

[11] L. Clerc. Directional differences of impulse spread in trabecular muscle from mammalian heart. *Journal of Physiology*, 255:335–346, 1976.

[12] L. Tung. *A Bi–domain model for describing ischaemic myocardial D-C potentials.* PhD thesis, Massachusetts Institute of Technology, June 1978.

[13] W. T. Miller and D. B. Geselowitz. Simulation studies of the electrocardiogram I: The normal heart. *Circulation Research*, 43:301–315, 1978.

[14] R. Plonsey and R. C. Barr. A critique of impedance measurements in cardiac tissue. *Annals of Biomedical Engineering*, 14:307–322, 1986.

[15] S. Rush, J. A. Abildskov, and R. McFee. Resistivity of body tissues at low frequencies. *Circulation Research*, 12:40–50, 1963.

[16] A. van Oosterom, R. W. de Boer, and R. Th. Van Dam. Intramural resistivity of cardiac tissue. *Med. & Biol. Eng. & Comput.*, 17:337–343, 1979.

[17] R. Plonsey and R. C. Barr. The four-electrode resistivity technique as applied to cardiac muscle. *IEEE Transactions on Biomedical Engineering*, 29(7):541–546, 1982.

[18] P. Steendijk, G. Mur, E. T. van der Velde, and J. Baan. The four-electrode resistivity technique in anisotropic media: Theoretical analysis and application on myocardial tissue *in Vivo*. *IEEE Transactions on Biomedical Engineering*, 40(11):1138–1147, 1993.

[19] P. Le Guyader, F. Trelles, and P. Savard. Extracellular measurement of anisotropic bidomain myocardial conductivities. I. Theoretical analysis. *Annals of Biomedical Engineering*, 29:862–877, 2001.

[20] R. C. Barr and R. Plonsey. Electrode systems for measuring cardiac impedances using optical transmembrane potential sensors and interstitial electrodes — Theoretical design. *IEEE Transactions on Biomedical Engineering*, 50(8):925–934, 2003.

[21] P. Le Guyader, P. Savard, R. Guardo, L. Pouliot, F. Trelles, and M. Meunier. Myocardial impedance measurements with a modified four electrode technique. *16th IEEE-EMBS*, pages 880–881, 1994.

[22] P. Colli Franzone, L. Guerri, and B. Taccardi. Spread of excitation in a myocardial volume: Simulation studies in a model of anisotropic ventricular muscle activated by point stimulation. *Journal of Cardiovascular Electrophysiology*, 4(2):144–160, April 1993.

[23] I. J. LeGrice, P. J. Hunter, and B. H. Smail. Laminar structure of the heart: a mathematical model. *American Journal of Physiology*, 272:H2466–H2476, 1997.

[24] B. Taccardi, E. Macchi, R. L. Lux, P. R. Ershler, S. Spaggiari, S. Baruffi, and Y. Vyhmeister. Effect of myocardial fiber direction on epicardial potentials. *Circulation*, 90:3076–3090, 1994.

[25] D. D. Streeter. Gross morphology and fiber geometry of the heart. In R. M. Berne, editor, *Handbook of Physiology, Vol 1*, chapter 2: The Cardiovascular System, pages 61–112. Williams and Williams, Baltimore, MD, 1979.

[26] W. Krassowska and J.C. Neu. Effective boundary conditions for syncytial tissues. *IEEE Transactions on Biomedial Engineering*, 41(2):143–150, 1994.

[27] Peter R. Johnston. The effect of simplifying assumptions in the bidomain model of cardiac tissue: Application to ST-Segment Shifts During Partial Ischaemia. *Mathematical Biosciences*, 198(1):97–118, 2005.

[28] William H. Press, Brian P. Flannery, Saul A. Teukolsky, and William T. Vetterling. *Numerical Recipes, The Art of Scientific Computing*. Cambridge University Press, Cambridge, 2nd edition, 1992.

[29] R. W. Hamming. *Digital Filters*. Dover Publications Inc., New York, third edition, 1989.

[30] R. M. Gulrajani. *Bioelectricity and Biomagnetism*. John Wiley and Sons, 1998.

[31] B. J. Roth. Electrical conductivity values used with the bidomain model of cardiac tissue. *IEEE Transactions on Biomedical Engineering*, 44(4):326–328, April 1997.

[32] S. Weidmann. Electrical constants of trabecular muscle from mammalian heart. *J. Physiol.*, 210:1041–1054, 1970.

[33] B. M. Johnston and P. R. Johnston. An in-principle method for measuring cardiac tissue fibre rotation. In *Non-invasive functional source imaging*, pages 313–316, Minneapolis, USA, 2005.

[34] B. Taccardi, S. Veronese, P. Colli Franzone, and L. Guerri. Components in the unipolar electrogram: A simulation study in a three-dimensional model of ventricuar myocardium. *J Cardiovasc. Electrophysiol.*, 9:1062–1084, 1998.

[35] B. Taccardi, B.B. Punske, R.S. MacLeod, and Q. Ni. Extracardiac effects of myocardial electrical anisotropy. *J Biomedizinishe Technik*, 46:216–218, 2001.

[36] P. Colli Franzone, L. Guerri, M. Pennacchio, and B. Taccardi. Anisotropic mechanisms for multiphasic uniploar electrograms: Simulation studies and experimental recordings. *Annals of Biomedical Engineering*, 28:1326–1342, 2000.

[37] C. Ramon, P. Schimpf, Y. Wang, J. Haueisen, and A. Ishimaru. The effect of volume currents due to myocardial anisotropy on body surface potentials. *Phys. Med. Biol.*, 47:1167–1184, 2002.

[38] B. J. Roth. The electrical potential produced by a strand of cardiac muscle: A bidomain analysis. *Annals of Biomedical Engineering*, 16:609–637, 1988.

[39] Q. Li. *Transmyocardial ST potential distributions in ischaemic heart disease*. PhD thesis, University of Tasmania, 2005.

Captions

Figure 1: Schematic diagram for the surface four-probe configuration. Diagram is not to scale.

Figure 2: Normalised extracellular and intracellular potentials for positions on the four-electrode surface probe of Plonsey and Barr [17] for the numerical model and the analytic solution in the 'widely-spaced' electrode case.

Figure 3: Schematic diagram for the vertical probe configuration of Barr and Plonsey [20]. Open circles represent sites of optical transmembrane potential sensors, while closed circles represent sites of extracellular potential measurements. (a) Configuration for the 'closely-spaced' measurements. (b) Configuration for the 'widely-spaced' measurements. Diagrams are not to scale.

Figure 4: Normalised extracellular and intracellular potentials for positions on the four-electrode surface probe of Plonsey and Barr [17] for three different conductivity sets in the 'widely-spaced' electrode case.

Figure 5: Schematic diagram for the single vertical probe configuration. Diagram is not to scale.

Figure 6: Schematic diagram for the two-probe configuration. Diagram is not to scale.

Figure 7: Potential measured (in mV) for various depths and values of fibre rotation angle at a range of spacings between the two vertical probes.

Table 1: Conductivity parameters (in S/cm): (columns 1-3) experimentally determined; (columns 4-7) calculated using Roth [31] based on the mean value of g_{il} from columns 1-3.

Table 2: Extracellular and intracellular potentials at the measuring electrodes, found using the numerical model, for the four-electrode surface probe of Plonsey and Barr [17] for three different electrode spacings and three different sets of conductivity data.

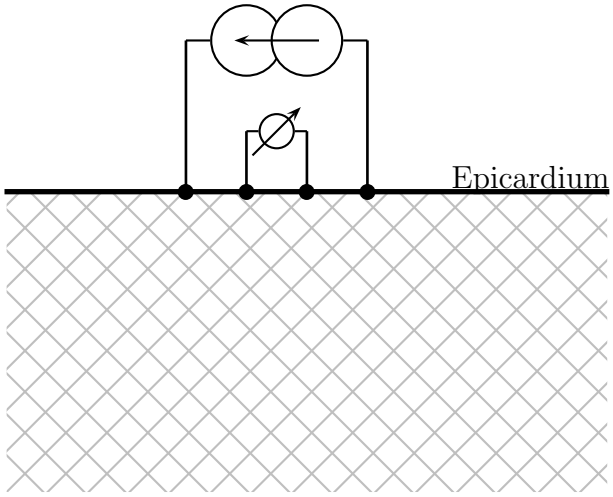

Figure 1:

	Clerc [11]	Roberts *et al.*[8]	Roberts and Sher[9]	Mean	Nominal	Equal	Reciprocal
g_{il}	0.00174	0.0028	0.0034	0.0026	0.0026	0.0026	0.0026
g_{it}	0.000193	0.00026	0.00060	0.00035	0.00026	0.00042	0.00021
g_{el}	0.00625	0.0022	0.0012	0.0032	0.0026	0.0026	0.0026
g_{et}	0.00236	0.0013	0.0008	0.0015	0.00104	0.00042	0.0322

Table 1:

	Φ_e (mV)			Φ_i (mV)		
	Equal	Nominal	Reciprocal	Equal	Nominal	Reciprocal
$0.1\lambda_w$	301.1	131.1	4.9	0.2	0.2	0.02
λ_w	28.9	11.7	0.4	1.7	1.3	0.1
$5\lambda_w$	3.8	1.7	0.06	2.3	1.7	0.1

Table 2:

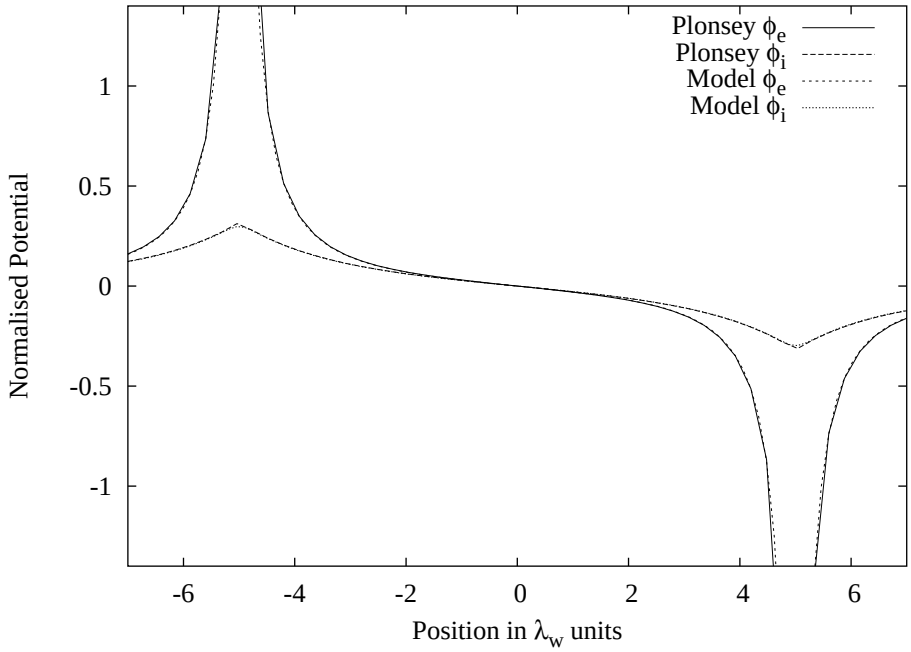

Figure 2:

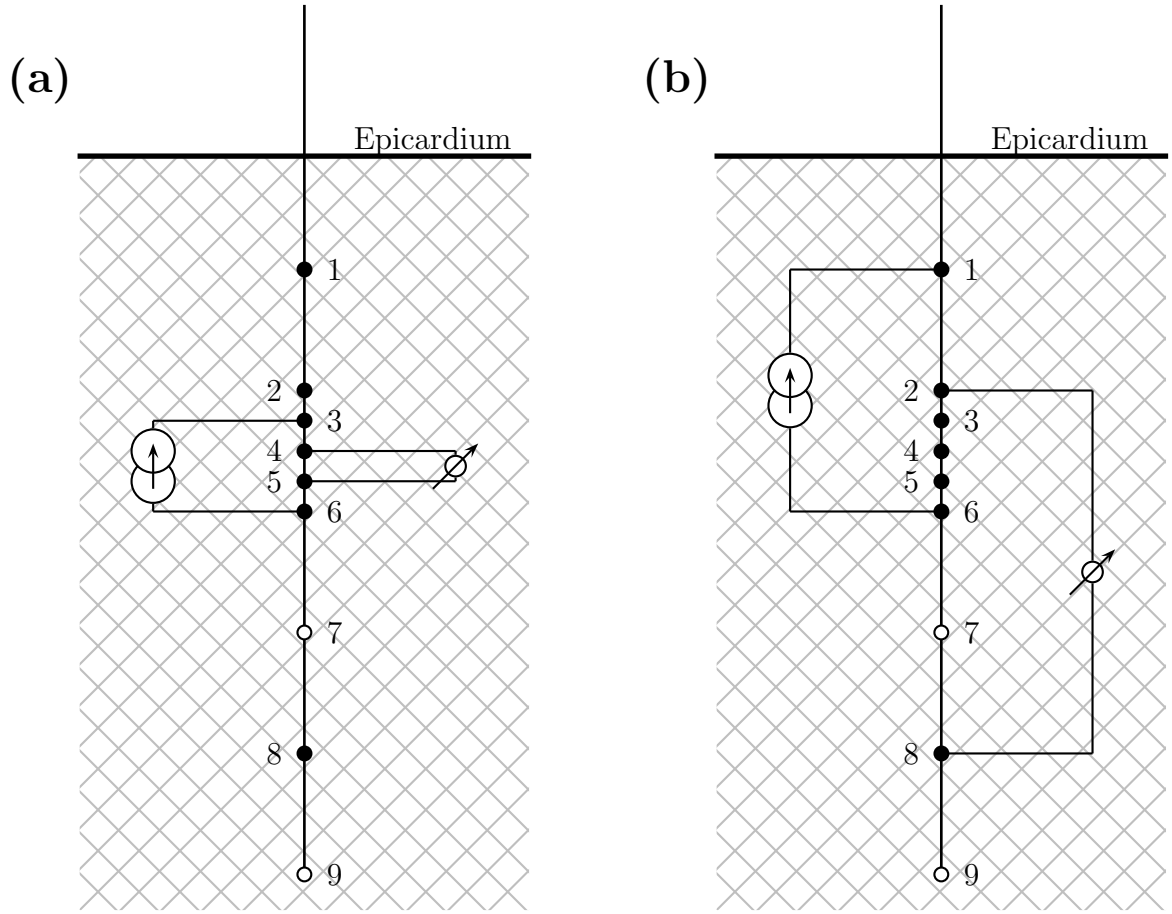

Figure 3:

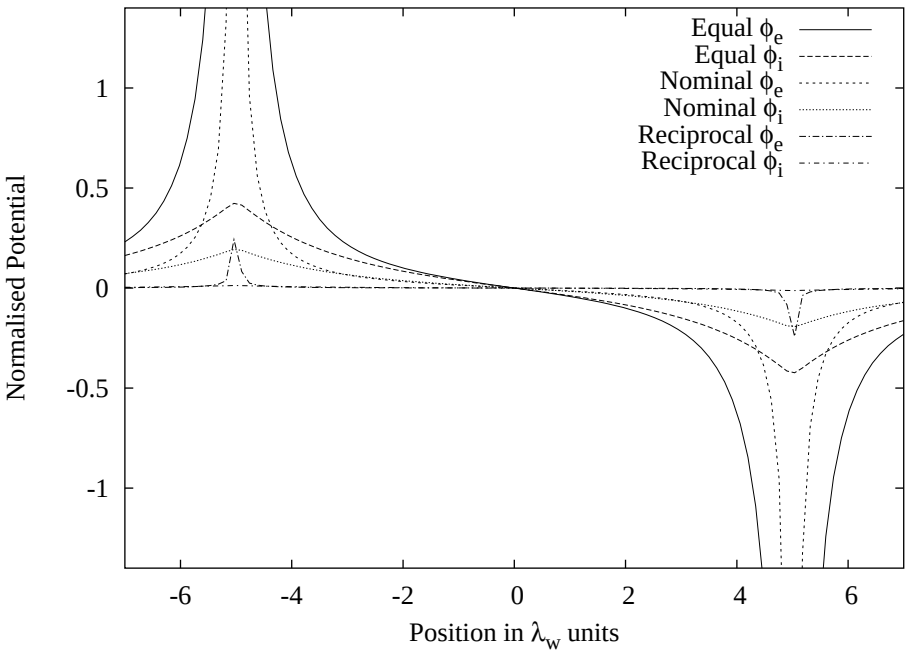

Figure 4:

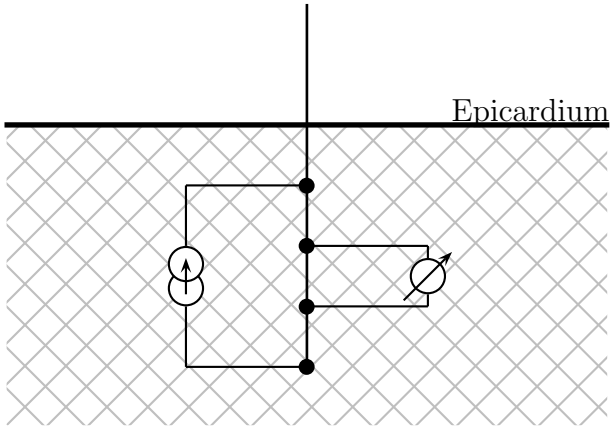

Figure 5:

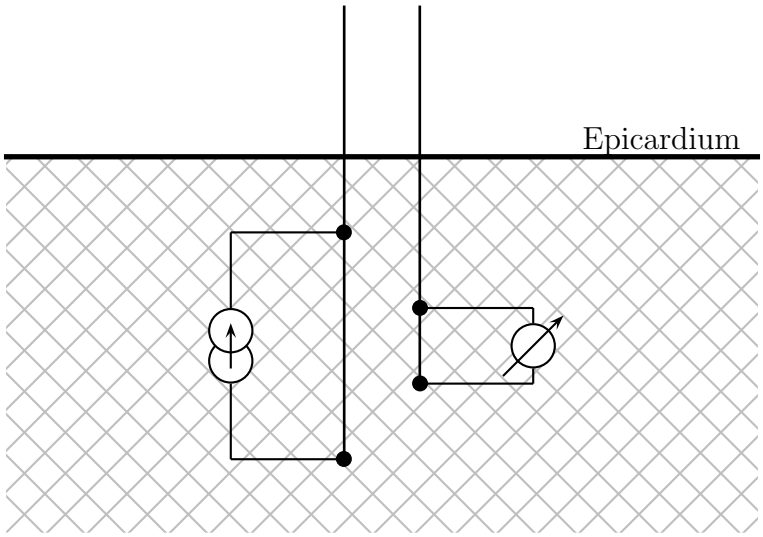

Figure 6:

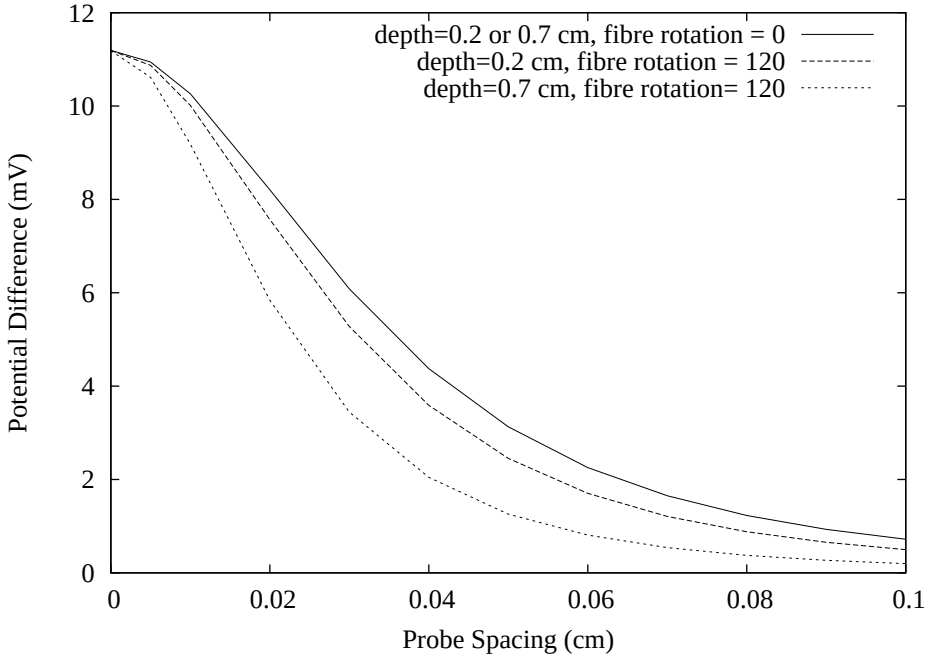

Figure 7: